Theory of Alfvén eigenmodes in shear reversed plasmas

B. N. Breizman, H. L. Berk, M. S. Pekker, S. D. Pinches, and S. E. Sharapov

Citation: Phys. Plasmas **10**, 3649 (2003); doi: 10.1063/1.1597495
View online: http://dx.doi.org/10.1063/1.1597495
View Table of Contents: http://pop.aip.org/resource/1/PHPAEN/v10/i9
Published by the American Institute of Physics.

Theory of Alfvén eigenmodes in shear reversed plasmas

B. N. Breizman, H. L. Berk, and M. S. Pekker
Institute for Fusion Studies, University of Texas at Austin, Austin, Texas 78712-1060

S. D. Pinches
Max-Planck Institut für Plasmaphysik, Euratom Association, Garching, Germany

S. E. Sharapov
Euratom/UKAEA Fusion Association, Culham Science Center, Abingdon, Oxfordshire OX14 3DB, United Kingdom

(Received 2 May 2003; accepted 28 May 2003)

Plasma configurations with shear reversal are prone to the excitation of unusual Alfvén eigenmodes by energetic particles. These modes exhibit a quasiperiodic pattern of predominantly upward frequency sweeping (Alfvén cascades) as the safety factor q changes in time. This work presents a theory that employs two complementary mechanisms for establishing Alfvén cascades: (1) a nonstandard adiabatic response of energetic particles with large orbits and (2) toroidal magnetohydrodynamic effects that are second-order in inverse aspect ratio. The developed theory explains the transition from Alfvén cascades to the toroidicity induced Alfvén eigenmodes (TAEs), including modifications of the TAEs themselves near the shear reversal point. © *2003 American Institute of Physics.* [DOI: 10.1063/1.1597495]

I. INTRODUCTION

There are several reasons why Alfvén eigenmodes are of interest in magnetic fusion research. The first is the concern that these modes can degrade energetic ion confinement,[1] particularly the confinement of fusion-produced alpha particles in burning plasma experiments.[2] The second is the observation that benign Alfvén eigenmodes can provide unique diagnostic opportunities via so-called magnetohydrodynamic-(MHD)-spectroscopy.[3] Finally, there is an impressive amount of high-quality and still not totally explained experimental data from various machines [Joint European Torus (JET), Tokamak Fusion Test Reactor (TFTR), JT-60U, DIII-D, and others] that necessitates a detailed theoretical analysis of the Alfvén modes themselves and of their interactions with the energetic ion population.

The shear Alfvén wave frequency range has been extensively explored in the experiments, with a particularly strong interest in toroidicity induced Alfvén eigenmodes (TAE).[4] The TAEs are associated with the gaps in the Alfvén continuum, which facilitates their excitation by reducing dissipation from continuum damping. The role of continuum damping would also be greatly reduced if modes arise at radial locations where there happens to be minimal spatial variation of the local shear Alfvén wave frequency,

$$\omega_A = \frac{V_A(r)}{R}\left(n - \frac{m}{q(r)}\right), \tag{1}$$

where n and m are the toroidal and the poloidal mode numbers, V_A is the Alfvén velocity, R is the major radius, and q is the safety factor. A good example of such a case is the global Alfvén eigenmode (GAE).[5,6] The frequencies of primary interest for many experiments are roughly of the order of the TAE frequency, $\omega_{\mathrm{TAE}} \equiv V_A/(2qR)$. When the mode numbers are substantially larger than unity it is apparent from Eq. (1) that such modes are more sensitive to the safety factor profile than they are to the plasma density profile. Thus any location where q is nearly flat should be viewed as a potential site for a shear Alfvén mode.

The aforementioned special role of flat q (zero shear) sites concurs with numerous observations of so-called Alfvén cascades (AC) in tokamak discharges with nonmonotonic q-profiles. The cascades were discovered on JT-60U (Ref. 7) and then also found on the JET,[8,9] where they have been studied extensively. The cascade modes typically appear in ''bunches.'' They emerge outside the TAE gap and exhibit a quasiperiodic pattern of frequency sweeping, as shown in Fig. 1. It has been revealed[10] that the mode frequencies actually trace the temporal evolution of ω_A due to the time dependence $q_0(t)$ of the safety factor at the zero shear point. However, the experiments exhibit only a subset of the frequencies described by Eq. (1). In particular, most of the observed frequencies move upward when the safety factor decreases in time. This feature indicates that some of the candidate frequencies given by Eq. (1) may not be suitable for establishing an eigenmode. It is also noteworthy that the allowed modes are not GAEs which would produce frequency sweeping in the opposite direction.

In order to establish the ''rules'' for the mode existence, one has to look specifically at the physics mechanisms that maintain the eigenmode structure. We note that in a plasma that is cold and spatially uniform there is a degeneracy in the shear Alfvén wave spectrum. In such a plasma, an arbitrary radial mode structure is compatible with the eigenfrequency determined by Eq. (1). The reason why the mode structure is not robust in this case is that different flux surfaces do not communicate via shear Alfvén signals. Two of the ways for them to communicate are via radial excursions of particle orbits (including gyro-orbits) and via toroidal MHD-effects.

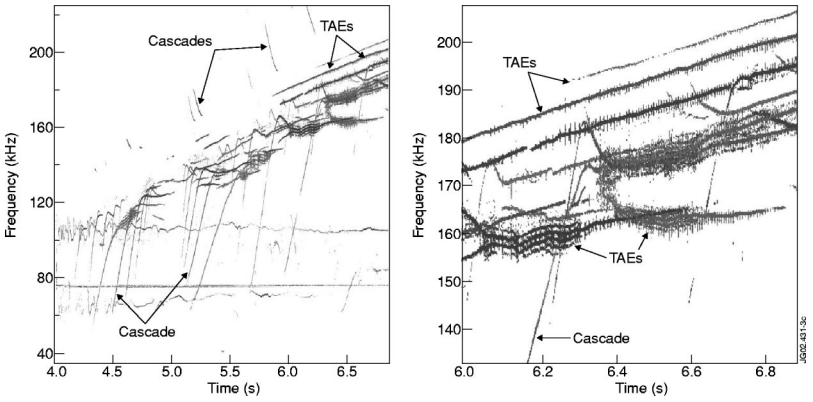

FIG. 1. Alfvén cascades of sweeping-up and of sweeping-down types, observed in a JET discharge simultaneously with TAEs. The right part of the figure is a zoom of the left part. It shows TAEs, some of which arise from the AC.

The first option was examined in Ref. 10 as a primary candidate for the interpretation of Alfvén cascades below the TAE gap in a plasma with a significant population of energetic particles. Here we examine the second option and demonstrate that the manifestation of toroidal MHD-effects away from the TAE gap is mathematically similar to that of the energetic particles, so that both effects can be conveniently described by the same eigenmode equation (see Sec. III). The closer to the TAE gap, the more significant is the role of coupling between the neighboring poloidal harmonics. However, the mode structure within the TAE gap differs considerably from that of conventional TAEs because the magnetic shear is very small at the mode location. In Sec. IV, we present a corresponding generalization of TAE theory. We also show that there is a continuous transformation of the Alfvén cascade modes into TAE modes as the safety factor changes in time at the shear reversal point. This transition is illustrated by the numerical results, presented in Sec. V.

In describing the ACs and TAEs we adopt a convention $n>0$ and consider waves with both positive and negative frequencies ω. These two cases correspond, respectively, to waves propagating along and opposite to the equilibrium toroidal magnetic field. The TAE dispersion relation is a function of only ω^2 so that both positive and negative frequency waves will exist. In contrast with TAEs, the AC dispersion relation contains linear dependence on ω, which breaks the symmetry between positive and negative frequencies, so that only waves of one particular sign of ω may exist. In order to identify all AC eigenmodes, the $\omega>0$ and $\omega<0$ cases will be investigated separately.

In the body of the text we describe the linear modes without regard to their excitation. Experimentally, the modes have been excited by a hot particle population, which introduces additional constraints on the observable modes. This issue will be discussed in Sec. VI. Once the relevant linearly unstable modes are identified, their saturation level in a weakly nonlinear regime can be calculated straightforwardly with the technique described in Ref. 11.

II. BASIC EQUATIONS

This section deals with a derivation of the eigenmode equations for shear Alfvén perturbations in a large-aspect-ratio torus. Our goal here is to present a formalism that we will then use to link Alfvén cascade modes to TAEs in plasmas with a nonmonotonic safety factor profile (i.e., with magnetic shear reversal). This formalism will also be relevant to the case of monotonic safety factor with an extended area of very low shear. For the sake of simplicity, we will restrict the derivation to the limiting case of zero plasma pressure and high mode numbers. We will therefore neglect all pressure effects in this paper. It should be pointed out that our equations will include second order corrections in inverse aspect ratio. We will then demonstrate (in Sec. III) that these corrections alone can support a localized mode below the TAE gap if the magnetic shear is sufficiently low.

We choose a gauge in which the scalar potential equals zero, so that the perturbed electric and magnetic fields can be written in terms of a vector potential δA as follows:

$$\delta \boldsymbol{E} = -\frac{1}{c}\frac{\partial \delta \boldsymbol{A}}{\partial t}, \quad \delta \boldsymbol{B} = \mathrm{curl}\ \delta \boldsymbol{A}. \tag{2}$$

We assume that the parallel component of the perturbed electric field vanishes due to high electron conductivity along the magnetic field lines. The perturbed vector potential $\delta \boldsymbol{A}$ can then be represented by a single scalar function Φ,

$$\delta \boldsymbol{A} = \nabla \Phi - \boldsymbol{b}(\boldsymbol{b}\cdot\nabla\Phi), \tag{3}$$

where $\boldsymbol{b} \equiv \boldsymbol{B}/B$ is a unit vector in the direction of the equilibrium magnetic field $\boldsymbol{B}$. This representation eliminates compressional Alfvén perturbations that would otherwise be described by another scalar function, Ψ, with an additional term $\nabla\Psi\times\boldsymbol{b}$ on the right-hand side of Eq. (3). The shear Alfvén mode equation for Φ comes from the quasineutrality condition,

$$\mathrm{div}\ \delta \boldsymbol{j}_{\parallel} + \mathrm{div}\ \delta \boldsymbol{j}_{\perp} = 0, \tag{4}$$

where $\delta \boldsymbol{j}_{\parallel}$ and $\delta \boldsymbol{j}_{\perp}$ are the components of the perturbed current (parallel and perpendicular to the direction of the equilibrium magnetic field, respectively). The perturbed parallel current is related to Φ by the Ampère law,

$$\delta \boldsymbol{j}_{\parallel} = \frac{c}{4\pi}\boldsymbol{b}(\boldsymbol{b}\cdot\mathrm{curl}\ \delta \boldsymbol{B})$$

$$= -\frac{c}{4\pi}\boldsymbol{b}(\boldsymbol{b}\cdot\mathrm{curl}\,\mathrm{curl}(\boldsymbol{b}(\boldsymbol{b}\cdot\nabla\Phi))). \tag{5}$$

Calculation of the perturbed perpendicular current involves the momentum balance equation,

$$\rho\frac{\partial\delta\boldsymbol{v}}{\partial t}=\frac{1}{c}[\,\delta\boldsymbol{j}\times\boldsymbol{B}]+\frac{1}{4\pi}[\,\mathrm{curl}\,\boldsymbol{B}\times\delta\boldsymbol{B}] \tag{6}$$

with

$$\delta\boldsymbol{v}_{\perp}=-\frac{c}{B}[\boldsymbol{b}\times\delta\boldsymbol{E}]=\frac{1}{B}[\boldsymbol{b}\times\nabla\dot{\Phi}]. \tag{7}$$

Substitution of $\delta\boldsymbol{j}_{\parallel}$ and $\delta\boldsymbol{j}_{\perp}$ into Eq. (4), with some additional straightforward algebra, gives

$$\begin{aligned}&\mathrm{div}\frac{1}{V_A^2}\left[\boldsymbol{b}\times\left[\nabla\frac{\partial^2\Phi}{\partial t^2}\times\boldsymbol{b}\right]\right]\\&=(\boldsymbol{B}\cdot\nabla)\frac{1}{B^2}\mathrm{div}\left[\boldsymbol{B}\times\left[\mathrm{grad}\left(\frac{1}{B}(\boldsymbol{b}\cdot\nabla\Phi)\right)\times\boldsymbol{B}\right]\right]\\&\quad-\mathrm{grad}\left(\frac{1}{B}(\boldsymbol{b}\cdot\nabla\Phi)\right)\cdot\nabla^2\boldsymbol{B}\\&\quad+(\boldsymbol{B}\cdot\nabla)\left[\frac{1}{B^2}\left(\frac{1}{B}(\boldsymbol{b}\cdot\nabla\Phi)\right)(\boldsymbol{B}\cdot\nabla^2\boldsymbol{B})\right],\end{aligned} \tag{8}$$

where V_A is the Alfvén velocity. We will limit our consideration to modes with a global scale-length along the magnetic field lines but with large poloidal and toroidal mode numbers n and m. We therefore neglect the last term on the right-hand side of Eq. (8) and obtain

$$\begin{aligned}\hat{L}\Phi\equiv&-\mathrm{div}\frac{1}{V_A^2}\left[\boldsymbol{b}\times\left[\nabla\frac{\partial^2\Phi}{\partial t^2}\times\boldsymbol{b}\right]\right]\\&+(\boldsymbol{B}\cdot\nabla)\frac{1}{B^2}\mathrm{div}\left[\boldsymbol{B}\times\left[\mathrm{grad}\left(\frac{1}{B}(\boldsymbol{b}\cdot\nabla\Phi)\right)\times\boldsymbol{B}\right]\right]\\&-\mathrm{grad}\left(\frac{1}{B}(\boldsymbol{b}\cdot\nabla\Phi)\right)\cdot\nabla^2\boldsymbol{B}=0,\end{aligned} \tag{9}$$

where we have introduced a self-explanatory linear differential operator $\hat{L}$ to shorten the forthcoming calculations.

Our analysis of Eq. (9) in an axisymmetric torus will employ straight field-line coordinates with the following expression for the unperturbed magnetic field:

$$\boldsymbol{B}=B_0\frac{r}{q(r)}\nabla r\times\nabla(q\theta-\zeta), \tag{10}$$

where ζ and θ are the toroidal and poloidal angles, respectively, r is the flux coordinate, $q(r)$ is the safety factor, and B_0 is the value of the unperturbed field on the magnetic axis. The Jacobian J and the metric coefficients for this coordinate system in a large aspect ratio tokamak are given in Appendix A.

The function Φ, which is a periodic function of ζ and θ, can be represented by a Fourier series as follows:

$$\Phi(r;\theta;\zeta;t)=\exp(in\zeta-i\omega t)\sum_m\ \Phi_m(r)\exp(-im\theta)+\mathrm{c.c.}, \tag{11}$$

where ω is the mode frequency, and $\Phi_m(r)$ is the radial eigenfunction for the mth poloidal harmonic.

An important feature of the low shear eigenmodes is that each of them contains no more than three significant poloidal harmonics, so that we can truncate the right-hand side of Eq. (11) to just three terms. We will label these terms by the subscripts $m-1$, m, and $m+1$ respectively, reflecting the fact that the toroidal effects couple primarily the neighboring harmonics. The corresponding three equations for $\Phi_{m-1}(r),\Phi_m(r)$, and $\Phi_{m+1}(r)$ will be further reduced to either a single equation for $\Phi_m(r)$ (if the mode frequency is not too close to the TAE gap) or to a set of two coupled equations for $\Phi_{m-1}(r)$ and $\Phi_m(r)$ (if the mode frequency is within the TAE gap or very close to the gap).

In order to derive the equations for $\Phi_{m-1}(r)$, $\Phi_m(r)$, and $\Phi_{m+1}(r)$ we multiply Eq. (9) by $(J/R_0)\exp(-in\zeta+i\omega t+il\theta)$, where the integer l runs from $m-1$ through $m+1$, and we average the result over the angular variables $(\zeta;\theta)$ and over time. It is convenient to write the ensuing equations in a matrix form,

$$\hat{L}_{l;j}\Phi_j(r)=0, \tag{12}$$

where summation over j is implied with j running from $m-1$ through $m+1$. The matrix $\hat{L}_{l;j}$ is related to the operator $\hat{L}$ by

$$\hat{L}_{l;j}\equiv\frac{1}{R_0}\langle J(r;\theta)\exp(il\theta)\hat{L}\exp(-ij\theta)\rangle, \tag{13}$$

where the angular brackets denote the poloidal angle averaging procedure. Every element of the matrix $\hat{L}_{l;j}$ is a second-order differential operator in r. The explicit expressions for these operators are presented in Appendices B and C.

Our treatment of Eq. (12) will employ characteristic ordering features of the operators $\hat{L}_{l;j}$ in a large-aspect-ratio tokamak. We observe that all the off-diagonal operators are proportional to the inverse aspect ratio, which makes them generally smaller than any diagonal operator unless it is particularly close to $\Omega_l\equiv V_A/R\,|n-(1/q)|$ for any of the three allowed l-values. Furthermore, it is allowable to drop the operators $\hat{L}_{m-1;m+1}$ and $\hat{L}_{m+1;m-1}$ since the toroidicity-induced coupling between the poloidal harmonics involves primarily the closest neighbors. If the frequencies Ω_{m-1},Ω_m, and Ω_{m+1} are all significantly different (for a given value of q), then only one of the diagonal operators can be uncharacteristically small. It is also possible that two of the three diagonal operators become small simultaneously but this requires that the corresponding frequencies come close to each other. The case of well-separated Ω_l (i.e., frequencies sufficiently far from the TAE gaps) is relevant to cascade modes, whereas the other case represents TAE modes. In what follows, we first consider each of these two cases separately and then describe the transition between the two.

III. CASCADE MODES

In this subsection, we will assume that the only ''small'' diagonal operator is $\hat{L}_{m;m}$. We then transform Eq. (12) to the following set:

$$\hat{L}_{m;m}\Phi_m(r)+\hat{L}_{m;m-1}\Phi_{m-1}(r)+\hat{L}_{m;m+1}\Phi_{m+1}(r)=0, \tag{14}$$

$$\Phi_{m-1}(r) = -\hat{L}^{-1}_{m-1;m-1}[\hat{L}_{m-1;m}\Phi_m(r)], \tag{15}$$

$$\Phi_{m+1}(r) = -\hat{L}^{-1}_{m+1;m+1}[\hat{L}_{m+1;m}\Phi_m(r)], \tag{16}$$

where the superscript ''-1''denotes an inverse operator. The inversion is a suitable procedure for the ''large'' operators ($\hat{L}_{m-1;m-1}$ and $\hat{L}_{m+1;m+1}$) since it does not introduce ''small denominators.'' We thereby reduce Eqs. (14)–(16) to a single equation for $\Phi_m(r)$,

$$\hat{L}_{m;m}\Phi_m(r) = \hat{L}_{m;m-1}\{\hat{L}^{-1}_{m-1;m-1}[\hat{L}_{m-1;m}\Phi_m(r)]\} + \hat{L}_{m;m+1}\{\hat{L}^{-1}_{m+1;m+1}[\hat{L}_{m+1;m}\Phi_m(r)]\}. \tag{17}$$

It is remarkable that, for the problem of interest, this equation is actually equivalent to a second order differential equation despite the fact that the term on the right-hand side is generally an integrodifferential operator. We find that the only difference between Eq. (17) and a similar second order differential equation,

$$\hat{L}_{m;m}\Phi_m(r) = 0, \tag{18}$$

is in the coefficients that describe the ε^2-corrections to this otherwise ''cylindrical'' eigenmode equation.

In order to explicitly calculate the right-hand side contribution to Eq. (17), we note that each of the two terms on the right-hand side is already quadratic in the inverse aspect ratio. It is therefore allowable to treat all the coefficients in the operators on the right-hand side as constants as long as the function $\Phi_m(r)$ is localized in the vicinity of the zero shear point and the radial width of $\Phi_m(r)$ is much smaller than the minor radius. In addition, it is allowable to use the lowest order dispersion relation,

$$\omega^2 = \omega_0^2 \equiv \frac{\overline{V}_A^2}{R_0^2}\left(n - \frac{m}{q_0}\right)^2, \tag{19}$$

to simplify the right-hand side of Eq. (17) since small deviations from this relation can be safely ignored in the ε^2-corrections. The quantity $\overline{V_A}$ in Eq. (19) is the flux surface averaged Alfvén velocity, as defined in Appendix C. The described simplifications allow us to straightforwardly calculate the right-hand side of Eq. (17) via Fourier transformation in radius. We then convert the Fourier image back into a real space representation to obtain

$$\begin{aligned}
&\hat{L}_{m;m-1}\{\hat{L}^{-1}_{m-1;m-1}[\hat{L}_{m-1;m}\Phi_m(r)]\} \\
&\quad + \hat{L}_{m;m+1}\{\hat{L}^{-1}_{m+1;m+1}[\hat{L}_{m+1;m}\Phi_m(r)]\} \\
&\quad = 2r\frac{\omega^2}{\overline{V}_A^2}\left\{\frac{\partial^2}{\partial r^2}\left[\frac{(\Delta'+\varepsilon)^2}{(2qn-2m)^2-1} + \varepsilon(2\Delta'+\varepsilon)\right]\right. \\
&\qquad \left. - \left(\frac{m}{r}\right)^2\left[\frac{(\Delta')^2}{(2qn-2m)^2-1} - \varepsilon(2\Delta'+\varepsilon)\right]\right\}\Phi_m .
\end{aligned} \tag{20}$$

Next, we combine Eq. (20) with a separately-derived expression for $\hat{L}_{m;m}\Phi_m(r)$ [see Eq. (B2)] and we rearrange the result by neglecting some of those ε^2-contributions that are only responsible for frequency redefinition (see Appendix B), which gives

$$\begin{aligned}
&\frac{\partial}{\partial r}\left[\frac{\omega^2}{\overline{V}_A^2} - \frac{1}{R_0^2}\left(n - \frac{m}{q}\right)^2\right] r\frac{\partial}{\partial r}\Phi_m - \frac{m^2}{r^2} \\
&\quad \times r\left[\frac{\omega^2}{\overline{V}_A^2}\left(1 + 2\frac{\varepsilon^2 + 2\Delta'\varepsilon}{(2qn-2m)^2-1}\right) - \frac{1}{R_0^2}\left(n - \frac{m}{q}\right)^2\right]\Phi_m \\
&\quad = 0.
\end{aligned} \tag{21}$$

In this equation, the toroidal effects, which shift the mode frequency from the Alfvén continuum, scale as ε^2, whereas the existence of toroidal Alfvén eigenmodes is associated with the linear in ε effects. Since the ε^2-terms that are responsible for the Alfvén cascades are quite small, one can expect that an energetic particle response may compete with the toroidicity effect in Eq. (21). Indeed, it was shown in Ref. 10 that fast ions themselves can be responsible for the existence of the Alfvén cascade mode. On the other hand, it is more difficult for the energetic particle response to compete with the $\mathcal{O}(\varepsilon)$ toroidicity effect associated with TAEs. By adding the theory developed in Ref. 10 to our analysis one finds that the contribution from the fast ions modifies the eigenmode equation to

$$\begin{aligned}
&\frac{d}{dr}\left[\frac{\omega^2}{\overline{V}_A^2} - \frac{1}{R_0^2}\left(n - \frac{m}{q}\right)^2\right] r\frac{d}{dr}\Phi_m \\
&\quad - \frac{m^2}{r^2}r\left[\frac{\omega^2}{\overline{V}_A^2} - \frac{1}{R_0^2}\left(n - \frac{m}{q}\right)^2\right]\Phi_m \\
&\quad = \frac{m^2}{r^2}r\frac{\omega^2}{\overline{V}_A^2}\left(2\frac{\varepsilon^2 + 2\varepsilon\Delta'}{(2qn-2m)^2-1}\right)\Phi_m + \frac{4\pi e}{cB}m\Phi_m \\
&\qquad \times \frac{d}{dr}\left[\omega\langle n_h\rangle - \frac{1}{eR_0}\left(n - \frac{m}{q}\right)\langle j_{\|h}\rangle\right].
\end{aligned} \tag{22}$$

The angular brackets in this equation denote flux surface averaging, and the two contributions to the second term on the right-hand side represent the density and the parallel current of the fast ions, respectively. For the rest of the paper we assume a typical ion cyclotron resonance heating (ICRH) scenario, with $V_{\|\mathrm{hot}}/V_A \ll 1$, so that the energetic particle parallel current will be neglected.

In order to demonstrate the existence of an eigenmode in Eq. (22), we expand the parallel wave number parameter, $(1/R_0^2)(n - [m/q(r)])^2$, about the point of zero magnetic shear, $r = r_0$, where $q(r_0) \equiv q_0$ is the minimum value of the safety factor,

$$\begin{aligned}
\frac{1}{R_0^2}\left(n - \frac{m}{q(r)}\right)^2 &\cong \frac{1}{R_0^2}\left(n - \frac{m}{q_q}\right)^2 \\
&\quad + \frac{mq''(r)}{q_0^2}\frac{(r-r_0)^2}{R_0^2}\left(n - \frac{m}{q_0}\right).
\end{aligned} \tag{23}$$

We assume that this expression is accurate over a region Δr where the mode is localized, which requires $(\Delta r)^2 < |nq_0 - m|(q_0/mq_0'')$. We can then set $\omega = \omega_0$ and replace the coefficient in front of Φ_m on the right-hand side of Eq. (22) by its value at $r = r_0$ to obtain

$$\frac{d}{dx} D_m \frac{d\Phi_m}{dx} - D_m \Phi_m = 2 \frac{\omega_0^2 R_0^2 q_0^2}{\bar{V}_A^2} \frac{\varepsilon_0^2 + 2\varepsilon_0 \Delta_0'}{(2q_0 n - 2m)^2 - 1} \Phi_m + \frac{\omega_0^2 R_0^2 q_0^2}{\bar{V}_A^2} \frac{\omega_{ch}}{\omega_0} \frac{r_0}{m} \left(\frac{d\langle \rho_h \rangle}{\rho dr} \right)_{r=r_0} \Phi_m, \tag{24}$$

where $x \equiv (r - r_0)m/r_0$ is the normalized radial coordinate, ω_{ch} is the hot ion gyrofrequency, ρ_h and ρ are the hot ion and the bulk plasma mass densities, and the quantity $D_m(x)$ is given by

$$D_m(x) = \left[2(\omega - \omega_0)\omega_0 \frac{q_0^2 R_0^2}{\bar{V}_A^2} - (q_0 n - m) \frac{r_0^2 q_0''}{q_0 m} x^2 \right]. \tag{25}$$

Equation (24) has exactly the same structure as Eq. (12) in Ref. 10, where the Alfvén cascades due to the hot ions alone were described. We can then immediately generalize the mode existence criterion from Ref. 10 to the following inequality:

$$Q_{\text{eff}} \equiv Q_{\text{hot}} + Q_{\text{tor}} > 1/4, \tag{26}$$

where

$$Q_{\text{hot}} = \left(-\frac{d\langle n_h \rangle}{dr} \right)_{r=r_0} \frac{4\pi e R_0^2 q_0^3}{cBr_0 q_0''} \frac{\omega_0}{(m - nq_0)} \equiv \omega_0^2 \frac{q_0^2 R_0^2}{\bar{V}_A^2 (m - nq_0)} \frac{q_0}{r_0^2 q_0''} \left[\left(-\frac{r}{\rho} \frac{d\langle \rho_h \rangle}{dr} \right)_{r=r_0} \frac{\omega_{ch}}{\omega_0} \right], \tag{27}$$

is the hot ion contribution introduced in Ref. 10, and

$$Q_{\text{tor}} = m\omega_0^2 \frac{2q_0^2 R_0^2}{\bar{V}_A^2 (m - nq_0)} \frac{q_0}{r_0^2 q_0''} \frac{\varepsilon_0(\varepsilon_0 + 2\Delta_0')}{[1 - (2q_0 n - 2m)^2]} \tag{28}$$

is a geometric contribution due to toroidicity.

We note that for a given value of q_0, Eq. (24) can describe cascade modes with different m-values and with different frequencies (either above or below the TAE gap). In preparation to our subsequent discussion of the transition from the cascades to TAEs (see Sec. V), we select two neighboring m-values (M and $M-1$) and we consider the range $M/n > q_0 > (M-1)/n$ with an exception of a small area around $q_{\text{TAE}} = (M-1/2)/n$ [where Q_{tor} becomes singular and the cascade approximation used to derive Eq. (24) breaks down]. In order to identify all the cascade modes that are possible as q_0 varies, we turn to Fig. 2, which shows schematically the normalized mode frequencies $\Omega = \omega/\omega_{\text{TAE}}$ as a function of q_0 in the range of interest. Figure 2(a) is for $\omega > 0$ and Fig. 2(b) is for $\omega < 0$. Each figure is divided into quadrants, depending on signs of Q_{tor} and Q_{hot} for the corresponding m-value. The characterization of each quadrant, starting at the lower left corner and moving clockwise is as follows:

(a) $M/n > q_0 > (M-1/2)/n$; $|\Omega| < 1$, $m = M$,
(b) $M/n > q_0 > (M-1/2)/n$; $|\Omega| > 1$, $m = M-1$,
(c) $(M-1/2)/n > q_0 > (M-1)/n$; $|\Omega| > 1$, $m = M$,
(d) $(M-1/2)/n > q_0 > (M-1)/n$; $|\Omega| < 1$, $m = M-1$.

The solid curves in Fig. 2 indicate how the cascade mode frequency varies when the frequency is sufficiently far from the TAE gap assuming that the condition (26) is satisfied. Clearly, there cannot be a cascade mode in the quadrants where both Q_{tor} and Q_{hot} are negative. Both Q_{tor} and Q_{hot} are positive in quadrant (a) for $\omega > 0$ and in quadrant (b) for $\omega < 0$, so that in these quadrants both effects help support a

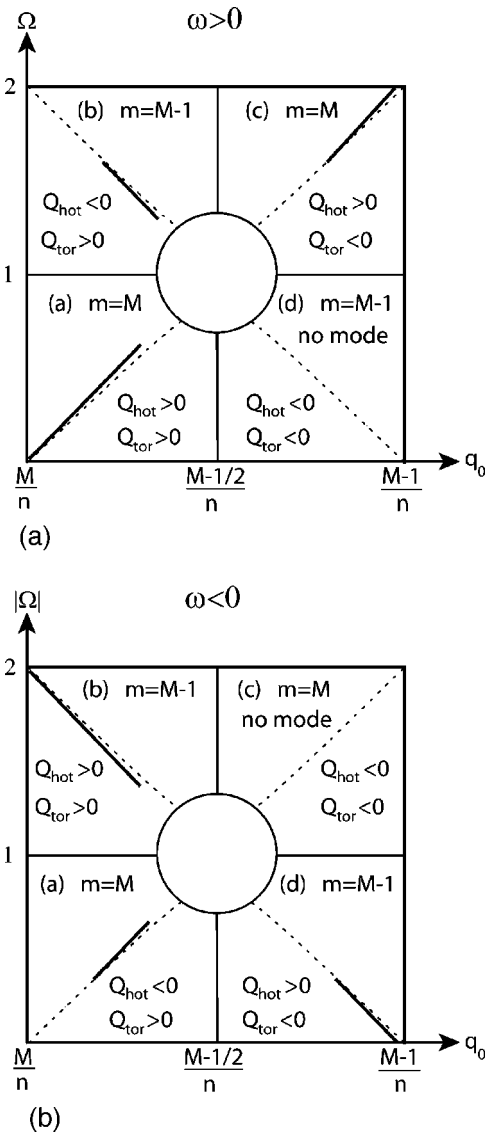

FIG. 2. Schematic plot of the AC mode frequencies for two selected poloidal mode numbers M and $M-1$. The different quadrants correspond to different signs of Q_{hot} and Q_{tor}. Solid lines indicate possible AC modes, dashed lines indicate the Alfvén continuum, the circles indicate the regions where the cascade mode approximation fails. The relevant values of m are shown in each quadrant. (a) represents positive frequencies and (b) is for negative frequencies.

cascade mode. To have a cascade mode in the other quadrants requires one of the Q-values to be sufficiently larger than the other to satisfy Eq. (26).

The spectrum of eigenfrequencies for Eq. (24) is described in Ref. 10. To apply that theory here we only need to replace the quantity Q of Ref. 10 by $Q_{\rm hot}+Q_{\rm tor}$. It is also instructive to apply a WKB analysis to Eq. (22) to infer the mode frequency shift from the Alfvén continuum (indicated in Fig. 2). We then find from Eq. (22),

$$k_r^2=\frac{m^2}{r^2}\left\{-1+\left[\frac{(\varepsilon^2+2\Delta'\varepsilon)}{[1-4(q_0n-m)^2]}-\frac{r}{2m}\frac{d\langle\rho_h\rangle}{\rho dr}\frac{\omega_{ch}}{\omega_0}\right]\times\frac{\omega_0^2q_0^2R_0^2}{[\omega_0(\omega-\omega_0)q_0^2R_0^2+\bar{V}_A^2m(m-nq_0)(q-q_0)]}\right\}, \tag{29}$$

where k_r is the radial wave number. To obtain a mode in WKB theory, we need k_r^2 to be positive within a region of mode localization and to be negative outside this region. When $Q_{\rm tor}+Q_{\rm hot}>0$, the expression in the bracket can indeed be made positive for q in the vicinity of q_0 with a suitable choice of $(\omega-\omega_0)/\omega_0$. With a reversed shear profile, we see that $q-q_0$ increases away from the shear reversal surface, so that there are reflection points ($k_r^2=0$) on both sides of the surface, which is needed for a standing wave to exist. These WKB considerations lead to the frequency shifts of ω from ω_0 that are schematically shown in Fig. 2.

To conclude this section, we note down that it is not always necessary to have magnetic shear-reversal in the plasma to establish a mode outside the TAE gap. Even a monotonic safety factor profile can support such modes provided that this profile is sufficiently flat in the plasma core. This possibility arises in the absence of hot ions due to an interplay between the radial dependence in the ε-term in Eqs. (22) and (29) and the radial dependence in $q(r)$, which creates a "potential well" to support a radially localized eigenmode. To demonstrate this effect we note that the right-hand side of Eq. (29) can indeed be positive when $(\omega-\omega_0)$ and $q-q_0$ are sufficiently small. Note that $q-q_0$ is positive for a monotonically increasing q profile. Then, with $(\omega-\omega_0)/\omega_0$ small and positive the second term in the bracket is positive definite if $m/q_0-n>0$. We also note that this term is small near the origin [where ε and $r(d\langle\rho_h\rangle/dr)$ approach zero] and it is small far away from the origin (where $q-q_0$ is large). As a result, k_r^2 is negative in these bounding regions. In the intermediate region, k_r^2 can be made positive by a proper choice of ω, which indicates the existence of a radially-localized mode.

IV. TAEs NEAR SHEAR REVERSAL POINT

The role of toroidicity-induced coupling becomes crucial when the frequency of the cascade mode approaches the TAE gap. However, the conventional analytic description of TAEs does not cover the shear reversal case, which points out the need to modify the theory in order to accurately connect the cascade modes to TAEs.

The conventional TAE modes are known to be associated with "special" values of $q[q=q_{\rm TAE}\equiv(2m-1)/2n]$ that represent the strongest linear coupling between the mth and $(m-1)$th poloidal harmonics. Motivated by the experiments, we assume that the q-profile has a minimum at $q(r)=q_0$ within the plasma cross section and that q_0 decreases in time. In its motion, the lowest point in the q-profile can go from above to below $q_{\rm TAE}$. One might argue that there should be no TAE mode until q_0 reaches $q_{\rm TAE}$, and that there should be two modes when q_0 is below $q_{\rm TAE}$. However, the actual picture is more subtle as the TAEs do not emerge suddenly at the crossing. Instead, we find that there is a continuous transition from cascade-type modes to TAEs. The conventional TAE theory is insufficient to describe the transition because the shear is exactly zero at the crossing and the slope of the q-profile can no longer be treated as a constant at the mode location. A conceptually relevant approach to the case of very low shear was developed in Ref. 12, where it was pointed out that the radial mode width in this case is typically larger than the poloidal wavelength. Another important feature of the low shear case is the existence of multiple TAEs in the same gap. In what follows, we adapt the approach of Ref. 12 to address the transition from $q_0>q_{\rm TAE}$ to $q_0<q_{\rm TAE}$.

Only two of the three poloidal harmonics are significant in the TAE case. We will choose their poloidal mode numbers to be m and $m-1$. The essence of the problem is captured by the following set of equations for these two harmonics,

$$\frac{d}{dx}D_m\frac{d}{dx}\Phi_m-D_m\Phi_m+\frac{\varepsilon_0+\Delta_0'}{2}\Phi_{m-1}''-\frac{\varepsilon_0+2\Delta_0'}{2}\Phi_{m-1}'+\frac{\Delta_0'}{2}\Phi_{m-1}=0, \tag{30}$$

$$\frac{d}{dx}D_{m-1}\frac{d}{dx}\Phi_{m-1}-D_{m-1}\Phi_{m-1}+\frac{\varepsilon_0+\Delta_0'}{2}\Phi_m''+\frac{\varepsilon_0+2\Delta_0'}{2}\Phi_m'+\frac{\Delta_0'}{2}\Phi_m=0, \tag{31}$$

wherein $x\equiv(r-r_0)m/r_0$, the subscript "0" refers to the zero shear point, and the quantities D_m and D_{m-1} are given by

$$D_m=\left[\omega^2\frac{q_0^2R_0^2}{\bar{V}_A^2}-(q_0n-m)^2-(q_0n-m)\frac{r_0^2q_0''}{q_0m}x^2\right], \tag{32}$$

$$D_{m-1}=\left[\omega^2\frac{q_0^2R_0^2}{\bar{V}_A^2}-(q_0n-m+1)^2-(q_0n-m+1)\frac{r_0^2q_0''}{q_0m}x^2\right]. \tag{33}$$

For the radially-extended modes with a mode width $\Delta x\gg1$, we can formally treat all the derivative terms in these equations as small compared to nonderivative terms. This ap-

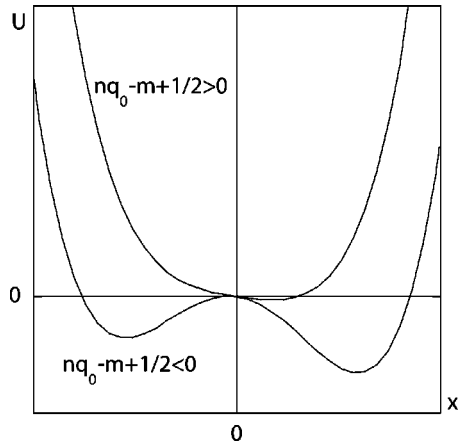

FIG. 3. Transformation of the effective potential for radially extended modes from a single well ($nq_0-m+1/2>0$) to a double well ($nq_0-m+1/2<0$).

proximation allows us to explicitly express Φ_{m-1} in terms of Φ_m and its derivatives and obtain a Schrödinger-type equation for Φ_m,

$$\frac{\varepsilon_0(\varepsilon_0+2\Delta_0')}{4}\frac{d^2\Phi_m}{dx^2}-\Phi_m\left[\left(1-2\left|nq_0-m+\frac{1}{2}\right|\right)\times\left(q_0n-m+\frac{1}{2}\right)\frac{r_0^2q_0''x^2}{q_0m}+\left(\frac{r_0^2q_0''x^2}{2q_0m}\right)^2+\frac{(\varepsilon_0+2\Delta_0')}{2}\frac{r_0^2q_0''x}{q_0m}\right]$$
$$=-\Phi_m\left\{\left[\frac{\omega^2q_0^2R_0^2}{\overline{V}_0^2}-(nq_0-m)^2\right]\times\left[\frac{\omega^2q_0^2R_0^2}{\overline{V}_A^2}-(nq_0-m+1)^2\right]-\left(\frac{\Delta_0'}{2}\right)^2\right\}. \quad (34)$$

We now observe that a change in q_0 from $q_0>q_{\mathrm{TAE}}$ to $q_0<q_{\mathrm{TAE}}$ changes the structure of the "potential energy" term from a single well to a double well, as shown in Fig. 3. The double-well case represents two preferred locations for TAEs on the opposite sides of the zero shear point. The single well case indicates that an eigenmode can exist even before q_0 crosses the value q_{TAE}. However, the long-wavelength approximation has a rather restrictive applicability condition in the single-well case. It requires $\varepsilon^3m \gg 4(q_0n-m+1/2)(r_0^2q_0''/q_0)$, which is difficult to satisfy unless the mode is very close to the TAE gap or the q-profile is nearly flat, so that $r_0^2q_0''\ll q_0$. The effects that allow the mode to survive outside the TAE gap have already been discussed in Sec. III.

V. TRANSITION FROM ALFVÉN CASCADES TO TAEs

In order to trace the transition from the nearly cylindrical cascade modes to TAEs we add the hot particle contribution Q_{hot} to the "diagonal" operators in Eqs. (12) and solve a truncated (two-harmonic) version of these equations numerically for a model reversed-shear equilibrium with circular flux surfaces. We choose a fixed radial profile of the toroidal current and vary the total value of the current, which changes the value of the safety factor at the zero shear point. This calculation gives a sequence of eigenfrequencies and radial eigenmodes for the selected values of q_0 as q_0 changes in time. This reduced numerical model has been verified with the full geometry codes MISHKA (Ref. 13) and CASTOR.[14] The long-wavelength approximation provides a relevant qualitative guidance for our numerical analysis.

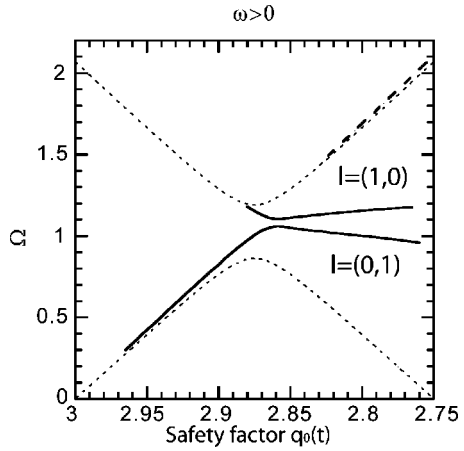

FIG. 4. Transition of Alfvén cascade modes to TAEs for positive frequency modes. Solid curves present eigenfrequencies for lowest order radial modes with $n=4$, $m=(12;11)$, and with the following values of input parameters: $r_0^2q_0''/q_0=0.25$, $Q_{\mathrm{hot}}=2$, $\varepsilon_0=0.13$, $\Delta_0'=0.03$. Thin dashed curves mark Alfvén continuum frequencies. Thick dashed curve represents the mode shown in quadrant (c) of Fig. 2(a).

Each calculated eigenmode can be labeled by its toroidal mode number n, a pair of poloidal mode numbers [assuming that the mode contains predominantly mth and $(m-1)$th poloidal components], and a radial label l, which is the number of zeros (nodes) in the radial eigenfunctions for each of the mth and $(m-1)$th poloidal components, respectively. Figures 4 and 5 show eigenfrequencies for lowest radial modes

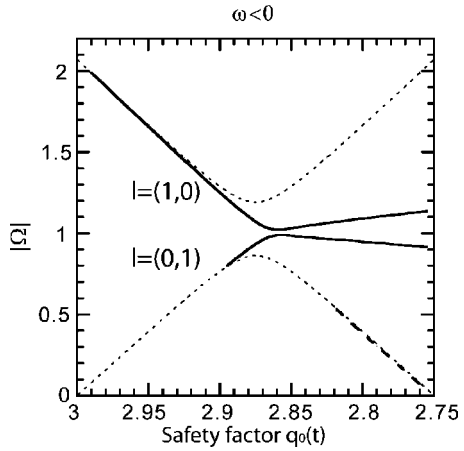

FIG. 5. Transition of Alfvén cascade modes to TAEs for negative frequency modes. Solid curves present eigenfrequencies for lowest order radial modes with $n=4$, $m=(12;11)$, and with the same input parameters as in Fig. 4. Thin dashed curves mark Alfvén continuum frequencies. Thick dashed curve represents the mode shown in quadrant (d) of Fig. 2(b).

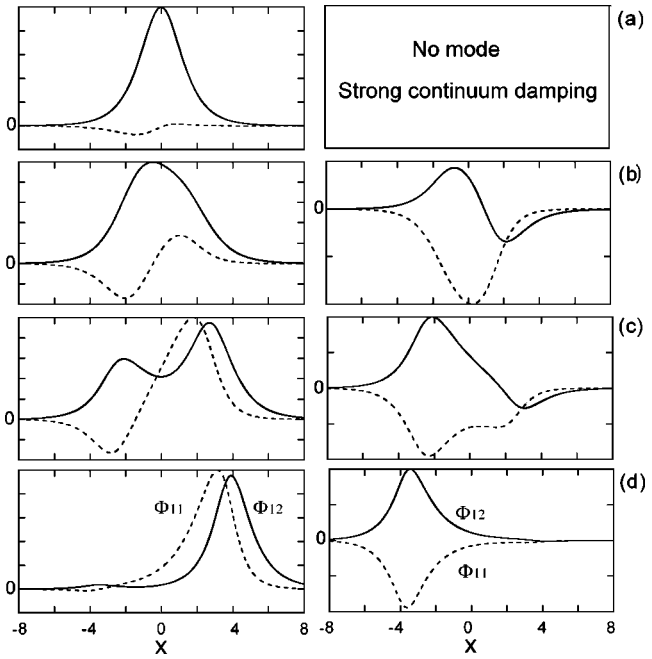

FIG. 6. Snapshots of the mode structure for a positive frequency mode with $n=4$ and $m=(12;11)$ during the transition from a cascade mode to TAE. The left column shows the radial profiles of the $m=12$ and $m=11$ poloidal components for the lower $[l=(0;1)]$ mode of Fig. 4. The right column shows the upper mode $[l=(1;0)]$. The values of q_0 for the snapshots are (a) $-q_0=2.915$; (b) $-q_0=2.875$; (c) $-q_0=2.86$; (d) $-q_0=2.84$.

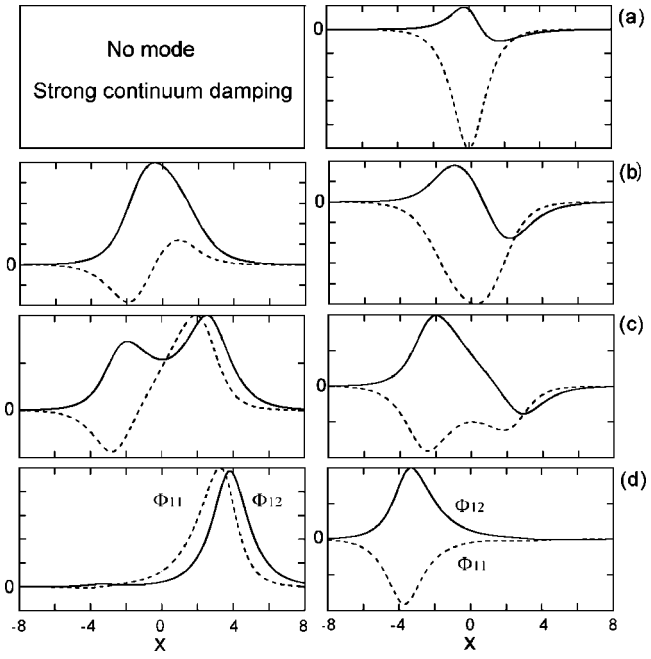

FIG. 7. Snapshots of the mode structure for a negative frequency mode with $n=4$ and $m=(12;11)$ during the transition from a cascade mode to TAE. The left column shows the radial profiles of the $m=12$ and $m=11$ poloidal components for the lower $[l=(0;1)]$ mode of Fig. 4. The right column shows the upper mode $[l=(1;0)]$. The values of q_0 for the snapshots are: (a) $-q_0=2.915$; (b) $-q_0=2.875$; (c) $-q_0=2.86$; (d) $-q_0=2.84$.

with the same values of n and m. The two solid curves trace the frequencies of the modes with $l=(0;1)$ (lower curve) and $l=(1;0)$ (upper curve) as a function of q_0. The dotted curves in the figure mark the Alfvén continuum frequencies for the selected values of n and m. This figure demonstrates a strong asymmetry in the mode frequency behavior: the mode first stays close to the continuum frequency until q_0 reaches q_{TAE}, and then detaches from the continuum and moves into the TAE gap rather than tracking the continuum which would reverse the direction of frequency chirping.

This pattern is consistent with the evolution of the potential well in Eq. (5), and the same general trend is clearly seen in the experimental data in Fig. 1. The calculated evolution of the mode structure along the solid curves of Figs. 4 and 5 provides additional evidence that the cascade modes indeed convert ''adiabatically'' into TAEs. Figure 6 illustrates how the initial cylindrical cascade mode with a poloidal mode number $m=12$ (indicated by the eigenfunction subscript) gains a second component due to toroidal coupling as the mode frequency approaches the TAE gap. Once in the gap, the mode then exhibits the typical signature of TAE, i.e., two nearly equal and strongly coupled poloidal components. Another characteristic feature in Fig. 6 is that the mode acquires a double-hump structure when the effective ''potential energy'' in Eq. (5) changes from a single well to a double well. Later in its evolution the Φ_{12}-component returns to a single hump structure that is now shifted from the zero shear point. The shift comes from an asymmetry of the double potential well, which forces the lower frequency mode to concentrate predominantly in one of the two adjacent wells. The upper frequency mode obviously ''prefers'' the other half of the well and it is therefore shifted to the left from the zero shear point. Also, the upper frequency mode has an antiballooning poloidal structure in the TAE gap (the opposite signs of the poloidal components cause mode localization on the inner part of the torus), whereas the lower frequency mode exhibits a ballooning structure (mode localization on the outer part of the torus). Figure 7 shows that negative frequency modes of Fig. 5 undergo a very similar transition in the mode structure.

VI. DISCUSSION AND SUMMARY

In this work we have extended the theory of Alfvén cascades[10] that have been observed in a variety of tokamak experiments with reversed magnetic shear. Initially their existence was attributed to the response of large orbit hot particles. The modified theory now includes toroidal MHD effects in addition to energetic particle effects. It demonstrates that the cascade modes can also exist without the energetic particles, although the energetic particles can substantially facilitate their manifestation. In addition, the extended theory predicts that the cascades can exist even without magnetic shear reversal if the q-profile is nearly flat in the center. The presented theory also describes the adiabatic transformation of Alfvén cascades into TAEs as well as modifications of TAEs themselves near the shear reversal point. It is pointed out that, for a given toroidal mode number, the Alfvén cascade spectrum accommodates both positive and negative frequency modes above and below the TAE range of frequencies.

In order to discuss experimental data when ACs and the TAEs are excited by energetic particles, an additional selection rule for the mode excitation needs to be applied. If one assumes that the excitation is due to the universal instability drive,[15] for an energetic particle profile that decreases radially then, in the notation of this paper, only the positive frequency waves should be selected. Nonetheless, it should be kept in mind that it is possible for the radial profile of the energetic particles to be inverted and that an additional instability drive due to hot particle anisotropy in phase space can conceivably lead to the excitation of the negative frequency waves.

As already pointed out, Fig. 1 demonstrates that the AC modes below the TAE frequency sweep upward when q_0 decreases in time. These modes are compatible with the case shown in quadrant (a) of Fig. 2(a). In this case the signs of both Q_{tor} and Q_{hot} are favorable for the existence of the mode and the universal instability mechanism provides a drive for the mode. We also see in Fig. 1 that some upward sweeping modes convert into TAEs, which is compatible with the behavior shown in Fig. 4, although in experiment there are cases where some modes disappear as the frequency reaches the TAE gap (a phenomenon that still needs explanation).

The cascade modes that start on top or above the TAE gap in Fig. 1 and sweep downward as q_0 decreases appear to be compatible with the mode shown in quadrant (b) of Fig. 2(a), where Q_{tor} is larger than $|Q_{\mathrm{hot}}|$. It still remains to determine why these downward sweeping modes terminate rather than gradually convert into TAEs.

The most recent theoretical discussion of the modes excited by the universal instability drive is presented in Ref. 16 that deals solely with the positive frequency modes. In the work presented here we have shown that the additional second order toroidal MHD effect allows for cascade modes to exist even without energetic particles. Also, the more complete spectrum of Alfvén modes that is described, which include negative and positive frequencies, can be employed in MHD spectroscopy[3] based on mode excitation with an external antennae. The observation that MHD effects alone can establish an AC eigenmode is particularly relevant to the experimental case with a very low density of hot ions, e.g., alpha-driven ACs in TFTR DT experiments with a nearly flat central q-profile.[17]

Both the detailed linear stability analysis and nonlinear theory of Alfvén cascades go beyond the limited scope of this paper. These extensions would be particularly desirable for diagnostic applications of Alfvén cascades. It is noteworthy that the cascades already provide a valuable diagnostic tool even at the present level of their understanding. An impressive example of that is the observed correlation between the cascades and the internal transport barrier (ITB) triggering events in reversed shear discharges in JET.[18] This correlation has been successfully used to optimize the discharge parameters for the transport barrier formation.[19]

ACKNOWLEDGMENTS

This work was supported by the U.S. Department of Energy Contract No. DE-FG03-96ER-54326, by The United Kingdom Engineering and Physical Sciences Research Council and by Euratom. The work was conducted partly under the European Fusion Development Agreement.

APPENDIX A: STRAIGHT FIELD LINE REPRESENTATION

In the straight field line representation [Eq. (10)], the three individual terms in Eq. (9) have the following form:

$$\begin{aligned}\mathrm{div}\frac{1}{V_A^2}\left[\boldsymbol{b}\times\left[\nabla\frac{\partial^2\Phi}{\partial t^2}\times\boldsymbol{b}\right]\right]&=\frac{1}{J}\frac{\partial}{\partial\theta}\left[J\frac{1}{V_A^2}\left[(\nabla\theta)^2\frac{\partial}{\partial\theta}\frac{\partial^2\Phi}{\partial t^2}+(\nabla r\cdot\nabla\theta)\frac{\partial}{\partial r}\frac{\partial^2\Phi}{\partial t^2}\right]\right]\\&+\frac{1}{J}\frac{\partial}{\partial r}\left[J\frac{1}{V_A^2}\left[(\nabla r)^2\frac{\partial}{\partial r}\frac{\partial^2\Phi}{\partial t^2}+(\nabla r\cdot\nabla\theta)\frac{\partial}{\partial\theta}\frac{\partial^2\Phi}{\partial t^2}\right]\right]\\&+\frac{1}{J}\frac{\partial}{\partial\zeta}\left[J\frac{1}{V_A^2}(\nabla\zeta)^2\frac{\partial}{\partial\zeta}\frac{\partial^2\Phi}{\partial t^2}\right]-\frac{B_0^2}{J}\left(\frac{\partial}{\partial\zeta}+\frac{1}{q}\frac{\partial}{\partial\theta}\right)\frac{1}{J}\frac{1}{B^2V_A^2}\left(\frac{\partial}{\partial\zeta}+\frac{1}{q}\frac{\partial}{\partial\theta}\right)\frac{\partial^2\Phi}{\partial t^2},\end{aligned}\tag{A1}$$

$$\begin{aligned}(\boldsymbol{B}\cdot\nabla)\frac{1}{B^2}\mathrm{div}\left[\boldsymbol{B}\times\left[\left(\frac{1}{B}(\boldsymbol{b}\cdot\nabla\Phi)\right)\times\boldsymbol{B}\right]\right]&=\frac{B_0}{J}\left(\frac{\partial}{\partial\zeta}+\frac{1}{q}\frac{\partial}{\partial\theta}\right)\frac{1}{B^2}\left\{\frac{1}{J}\frac{\partial}{\partial\theta}\left[JB^2\left[\frac{\partial F}{\partial\theta}(\nabla\theta)^2+\frac{\partial F}{\partial r}(\nabla r\cdot\nabla\theta)\right]\right]\right\}\\&+\frac{B_0}{J}\left(\frac{\partial}{\partial\zeta}+\frac{1}{q}\frac{\partial}{\partial\theta}\right)\frac{1}{B^2}\left\{\frac{1}{J}\frac{\partial}{\partial r}\left[JB^2\left[\frac{\partial F}{\partial r}(\nabla r)^2+\frac{\partial F}{\partial\theta}(\nabla r\cdot\nabla\theta)\right]\right]\right\}\\&+\frac{B_0}{J}\left(\frac{\partial}{\partial\zeta}+\frac{1}{q}\frac{\partial}{\partial\theta}\right)\frac{1}{B^2}\left\{\frac{1}{J}\frac{\partial}{\partial\zeta}\left[JB^2\frac{\partial F}{\partial\zeta}(\nabla\zeta)^2\right]\right.\\&\left.-\frac{B_0^2}{J}\left(\frac{\partial}{\partial\zeta}+\frac{1}{q}\frac{\partial}{\partial\theta}\right)\frac{1}{J}\left(\frac{\partial F}{\partial\zeta}+\frac{1}{q}\frac{\partial F}{\partial\theta}\right)\right\},\end{aligned}\tag{A2}$$

$$-\operatorname{grad} F\cdot\Delta\boldsymbol{B}=-\frac{\partial F}{\partial r}(\nabla r\cdot\Delta\boldsymbol{B})-\frac{\partial F}{\partial\theta}(\nabla\theta\cdot\Delta\boldsymbol{B})-\frac{\partial F}{\partial\zeta}(\nabla\zeta\cdot\Delta\boldsymbol{B}). \tag{A3}$$

In these expressions, the Jacobian J, the absolute value of the equilibrium magnetic field B, and the supplementary function F are given by

$$J\equiv\frac{1}{[\nabla r\times\nabla\theta]\cdot\nabla\zeta}, \tag{A4}$$

$$B^2\equiv B_0^2\left\{[(\nabla r)^2(\nabla\theta)^2-(\nabla r\cdot\nabla\theta)^2]+\frac{1}{q^2}[(\nabla r)^2(\nabla\zeta)^2]\right\}, \tag{A5}$$

$$F\equiv\frac{1}{B^2}(\boldsymbol{B}\cdot\nabla\Phi)=\frac{B_0}{JB^2}\left[\frac{\partial\Phi}{\partial\zeta}+\frac{1}{q}\frac{\partial\Phi}{\partial\theta}\right]. \tag{A6}$$

In a large aspect ratio tokamak with circular flux surfaces, the following expressions hold for the Jacobian and the metric coefficients:

$$J\equiv\frac{1}{[\nabla r\times\nabla\theta]\cdot\nabla\zeta}=rR_0\left(1+\frac{2r}{R_0}\cos\theta\right), \tag{A7}$$

$$\nabla r\cdot\nabla r=1+2\Delta'\cos\theta, \tag{A8}$$

$$\nabla\theta\cdot\nabla\theta=\frac{1}{r^2}\left[1-2\left(\frac{r}{R_0}+\Delta'\right)\cos\theta\right], \tag{A9}$$

$$\nabla r\cdot\nabla\theta=-\frac{\sin\theta}{r}\left(\frac{r}{R_0}+(r\Delta')'\right), \tag{A10}$$

$$\nabla\zeta\cdot\nabla\zeta=\frac{1}{R_0^2}\left(1-\frac{2r}{R_0}\cos\theta\right), \tag{A11}$$

$$\nabla r\cdot\nabla\zeta=\nabla\theta\cdot\nabla\zeta=0, \tag{A12}$$

wherein R_0 is the radius of the magnetic axis, $\Delta(r)$ is the Shafranov shift, and the prime denotes a radial derivative. In the absence of plasma pressure, Δ' is simply proportional to r for circular flux surfaces. It is therefore permissible to replace $(r\Delta')'$ by $2\Delta'$ in Eq. (A11) and in the subsequent expressions.

It should be noted that we have omitted all second-order terms in inverse aspect ratio in Eqs. (A8)–(A12). Nevertheless, it turns out that these expressions are still accurate enough for the calculation of the relevant ε^2-terms in the eigenmode equation. The only effect from the neglected contributions to Eqs. (A8)–(A12) is an insignificant renormalization of the eigenmode frequency.

APPENDIX B: DIAGONAL MATRIX ELEMENTS

The diagonal matrix elements ($\hat{L}_{m;m}$, $\hat{L}_{m-1;m-1}$, $\hat{L}_{m+1;m+1}$) are obtained by applying the averaging procedure [see Eq. (12)] to the components of the eigenmode equation described by Eqs. (A1)–(A3). Since $\nabla r\cdot\nabla\theta\propto\sin\theta$ is an odd function of θ, all the terms with $\nabla r\cdot\nabla\theta$ in Eqs. (A1)–(A3) vanish as a result of averaging. The remaining terms take the following form:

$$\hat{L}_{m;m}\Phi_m=\frac{\partial}{\partial r}\left\langle J\frac{\omega^2}{R_0V_A^2}(\nabla r)^2-\left(n-\frac{m}{q}\right)^2\frac{r^2}{R_0J}(\nabla r)^2\right\rangle\frac{\partial\Phi_m}{\partial r}-\frac{m^2}{r^2}\left\langle J\frac{\omega^2}{R_0V_A^2}(r\nabla\theta)^2-\left(n-\frac{m}{q}\right)^2\frac{r^2}{R_0J}(r\nabla\theta)^2\right\rangle\Phi_m. \tag{B1}$$

Equation (B1) implicitly includes the required $\mathcal{O}(\varepsilon^2)$ contributions in the inverse aspect ratio expansion. The neglected terms contain either an additional factor $(1/m)\ll 1$ or ε with respect to the retained $\mathcal{O}(\varepsilon^2)$ terms.

To zeroth order in ε, the quantities in the first and the second terms of Eq. (B1) are equal to each other. A vanishing bracket gives the Alfvén continuum dispersion relation. The geometrical toroidal corrections to the averaged expressions in angular brackets are $\mathcal{O}(\varepsilon^2)$ since the $\mathcal{O}(\varepsilon)$ terms are odd functions of θ. It should be pointed out that any small corrections that contribute equally to the two bracketed expressions do not affect the structure of Eq. (B1) as these corrections can be absorbed by a trivial redefinition of ω^2. We therefore need to select the corrections that create a difference between the bracketed terms. A simple analysis shows that all such corrections come only from the products of the linear (in ε) contributions to the Jacobian and to the metric coefficients. This observation means that the accuracy of Eqs. (A8)–(A10) is actually sufficient to calculate the required corrections. The resulting expression for the diagonal matrix element has the form,

$$\hat{L}_{m,m}=\frac{\partial}{\partial r}\left(\frac{\omega^2}{\overline{V_A^2}}(1+4\varepsilon\Delta')-\frac{(n-m/q)^2}{R_0^2}\right)r\frac{\partial}{\partial r}-\frac{m^2}{r}\left(\frac{\omega^2}{\overline{V_A^2}}(1-4\varepsilon(\varepsilon+\Delta'))-\frac{(n-m/q)^2}{R_0^2}\right). \tag{B2}$$

APPENDIX C: OFF-DIAGONAL MATRIX ELEMENTS

There are four off-diagonal elements that are relevant to the eigenmode equation. These are $\hat{L}_{m-1;m}$, $\hat{L}_{m;m-1}$, $\hat{L}_{m;m+1}$, and $\hat{L}_{m+1;m}$. Their evaluation involves the straightforward integration of the expression in Eq. (13) with $\hat{L}$ and J defined by Eqs. (9) and (A8). Only lowest order nonvanishing terms in inverse aspect ratio expansion need to be retained in these calculations. An additional simplification comes from the condition $m\gg 1$, which allows one to neglect

the difference between $m, m-1$ and $m+1$ everywhere except in the quantities $n-(m/q)$, $n-(m-1)/q$, and $n-(m+1)/q$ as these quantities are typically of the order of unity (not of the order of m) for the modes of interest. The resulting expressions for the off-diagonal elements are determined by the following equations:

$$\hat{L}_{m;m-1}\Phi_{m-1}=\frac{\partial}{\partial r}r(2\varepsilon+\Delta')\frac{\omega^2}{\overline{V}_A^2}\frac{\partial}{\partial r}\Phi_{m-1}-\frac{1}{R_0^2}\left(n-\frac{m}{q}\right)\frac{\partial}{\partial r}r\Delta'\frac{\partial}{\partial r}\left(n-\frac{m-1}{q}\right)\Phi_{m-1}$$
$$+\frac{\omega^2}{\overline{V}_A^2}\frac{\Delta'-\varepsilon}{r}m^2\Phi_{m-1}-\frac{1}{R_0^2}\frac{\Delta'+\varepsilon}{r}m^2\left(n-\frac{m-1}{q}\right)\left(n-\frac{m}{q}\right)\Phi_{m-1}$$
$$-\frac{\omega^2}{\overline{V}_A^2}m(\varepsilon+(r\Delta')')\frac{\partial}{\partial r}\Phi_{m-1}+\frac{1}{R_0^2}m\left(n-\frac{m}{q}\right)(\varepsilon+(r\Delta')')\frac{\partial}{\partial r}\left(n-\frac{m-1}{q}\right)\Phi_{m-1}, \tag{C1}$$

$$\hat{L}_{m;m+1}\Phi_{m+1}=\frac{\partial}{\partial r}r(2\varepsilon+\Delta')\frac{\omega^2}{\overline{V}_A^2}\frac{\partial}{\partial r}\Phi_{m+1}-\frac{1}{R_0^2}\left(n-\frac{m}{q}\right)\frac{\partial}{\partial r}r\Delta'\frac{\partial}{\partial r}\left(n-\frac{m+1}{q}\right)\Phi_{m+1}$$
$$+\frac{\omega^2}{\overline{V}_A^2}\frac{\Delta'-\varepsilon}{r}m^2\Phi_{m+1}-\frac{1}{R_0^2}\frac{\Delta'+\varepsilon}{r}m^2\left(n-\frac{m+1}{q}\right)\left(n-\frac{m}{q}\right)\Phi_{m+1}$$
$$+\frac{\omega^2}{\overline{V}_A^2}m(\varepsilon+(r\Delta)')\frac{\partial}{\partial r}\Phi_{m+1}-\frac{1}{R_0^2}m\left(n-\frac{m}{q}\right)(\varepsilon+(r\Delta')')\frac{\partial}{\partial r}\left(n-\frac{m+1}{q}\right)\Phi_{m+1}, \tag{C2}$$

$$\hat{L}_{m-1;m}\Phi_m=\frac{\partial}{\partial r}r(2\varepsilon+\Delta')\frac{\omega^2}{\overline{V}_A^2}\frac{\partial}{\partial r}\Phi_m-\frac{1}{R_0^2}\left(n-\frac{m-1}{q}\right)\frac{\partial}{\partial r}r\Delta'\frac{\partial}{\partial r}\left(n-\frac{m}{q}\right)\Phi_m+\frac{\omega^2}{\overline{V}_A^2}\frac{\Delta'-\varepsilon}{r}m^2\Phi_m$$
$$-\frac{1}{R_0^2}\frac{\Delta'+\varepsilon}{r}m^2\left(n-\frac{m-1}{q}\right)\left(n-\frac{m}{q}\right)\Phi_m+\frac{\omega^2}{\overline{V}_A^2}m(\varepsilon+(r\Delta')')\frac{\partial}{\partial r}\Phi_m$$
$$-\frac{1}{R_0^2}m\left(n-\frac{m-1}{q}\right)(\varepsilon+(r\Delta')')\frac{\partial}{\partial r}\left(n-\frac{m}{q}\right)\Phi_m, \tag{C3}$$

$$\hat{L}_{m+1;m}\Phi_m=\frac{\partial}{\partial r}r(2\varepsilon+\Delta')\frac{\omega^2}{\overline{V}_A^2}\frac{\partial}{\partial r}\Phi_m-\frac{1}{R_0^2}\left(n-\frac{m+1}{q}\right)\frac{\partial}{\partial r}r\Delta'\frac{\partial}{\partial r}\left(n-\frac{m}{q}\right)\Phi_m$$
$$+\frac{\omega^2}{\overline{V}_A^2}\frac{\Delta'-\varepsilon}{r}m^2\Phi_m-\frac{1}{R_0^2}\frac{\Delta'+\varepsilon}{r}m^2\left(n-\frac{m+1}{q}\right)\left(n-\frac{m}{q}\right)\Phi_m$$
$$-\frac{\omega^2}{\overline{V}_A^2}m(\varepsilon+(r\Delta')')\frac{\partial}{\partial r}\Phi_m+\frac{1}{R_0^2}m\left(n-\frac{m+1}{q}\right)(\varepsilon+(r\Delta')')\frac{\partial}{\partial r}\left(n-\frac{m}{q}\right)\Phi_m. \tag{C4}$$

In these expressions, we use a notation $\overline{V}_A$ for the flux surface averaged Alfvén velocity, which is the Alfvén velocity calculated for a local mass density $\rho(r)$ but for the on-axis magnetic field B_0. We retain the radial dependence of $\overline{V}_A(r)$ as well as the radial dependence of the inverse aspect ratio $\varepsilon \equiv r/R_0$, the Shafranov shift factor $\Delta'(r)$, and the safety factor $q(r)$.

[1] K. L. Wong, R. J. Fonck, S. F. Paul, D. R. Roberts, E. D. Fredrickson, R. Nazikian, H. K. Park, M. Bell, N. L. Bretz, R. Budny, S. Cohen, G. W. Hammett, F. C. Jobes, D. M. Meade, S. S. Medley, D. Mueller, Y. Nagayama, D. K. Owens, and E. J. Synakowski, Phys. Rev. Lett. **66**, 1874 (1991).
[2] ITER Physics Expert Group on Energetic Particles, Heating and Current Drive, ITER Physics Basis Editors, Nucl. Fusion **39**, 2471 (1999).
[3] J. P. Goedbloed, H. A. Holties, S. Poedts, G. T. A. Huysmans, and W. Kerner, Plasma Phys. Controlled Fusion **35**, B277 (1993); A. Fasoli, D.

Testa, S. Sharapov, H. L. Berk, B. N. Breizman, A. Gondhalekar, R. F. Heeter, M. Mantsinen, and contributors to the EFDA-JET Workprogramme, *ibid.* **44**, B159 (2002).
[4]C. Z. Cheng, L. Chen, and M. S. Chance, Ann. Phys. (N.Y.) **161**, 21 (1985); C. Z. Cheng and M. S. Chance, Phys. Fluids **29**, 3659 (1986).
[5]D. W. Ross, G. L. Chen, and S. M. Mahajan, Phys. Fluids **25**, 652 (1982).
[6]K. Appert, Plasma Phys. Controlled Fusion **24**, 1147 (1982).
[7]H. Kimura, Y. Kusama, M. Saigusa, G. J. Kramer, K. Tobita, M. Nemoto, T. Kondoh, T. Nishitani, O. Da Costa, T. Ozeki, T. Oikawa, S. Moriyama, A. Morioka, G. Y. Fu, C. Z. Cheng, and V. I. Afanas'ev, Nucl. Fusion **38**, 1303 (1998).
[8]S. E. Sharapov, D. Testa, B. Alper, D. N. Borba, A. Fasoli, N. C. Hawkes, R. F. Heeter, M. Mantsinen, M. G. Von Hellermann, and contributors to the EFDA-JET Workprogramme, Phys. Lett. A **289**, 127 (2001).
[9]S. E. Sharapov, B. Alper, H. L. Berk, D. N. Borba, B. N. Breizman, C. D. Challis, A. Fasoli, N. C. Hawkes, T. C. Hender, J. Mailloux, S. D. Pinches, D. Testa, and contributors to the EFDA-JET Workprogramme, Phys. Plasmas **9**, 2027 (2002).
[10]H. L. Berk, D. N. Borba, B. N. Breizman, S. D. Pinches, and S. E. Sharapov, Phys. Rev. Lett. **87**, 185002 (2001).
[11]H. L. Berk, B. N. Breizman, and M. S. Pekker, Plasma Phys. Rep. **23**, 778 (1997).
[12]J. Candy, B. N. Breizman, J. W. Van Dam, and T. Ozeki, Phys. Lett. A **215**, 299 (1996).
[13]G. T. A. Huysmans, S. E. Sharapov, A. B. Mikhailovskii, and W. Kerner, Phys. Plasmas **8**, 4292 (2001).
[14]W. Kerner, J. P. Goedbloed, G. T. A. Huysmans, S. Poedts, and E. Schwarz, J. Comput. Phys. **142**, 271 (1998).
[15]L. I. Rudakov and R. Z. Sagdeev, Sov. Phys. Dokl. **6**, 415 (1961).
[16]F. Zonca, S. Briguglio, L. Chen, S. Dettrick, G. Fogaccia, D. Testa, and G. Vlad, Phys. Plasmas **9**, 4939 (2002).
[17]R. Nazikian, G. J. Kramer, H. L. Berk, B. N. Breizman, and S. Sharapov, Bull. Am. Phys. Soc. **47**, 327 (2002).
[18]E. Joffrin, G. Gorini, C. D. Challis, N. C. Hawkes, T. C. Hender, D. F. Howell, P. Maget, P. Mantica, D. Mazon, S. E. Sharapov, G. Tresset, and contributors to the EFDA-JET Workprogramme, Plasma Phys. Controlled Fusion **44**, 1739 (2002).
[19]E. Joffrin, C. D. Challis, G. D. Conway, X. Garbet, A. Gude, S. Guenther, N. C. Hawkes, T. S. Hender, D. Howell, G. T. A. Huysmans, E. Lazzaro, P. Maget, M. Marachek, A. G. Peeters, S. D. Pinches, S. E. Sharapov, and contributors to the EFDA-JET Workprogramme, ''Internal transport barrier triggering by rational magnetic flux surfaces in tokamaks,'' *Fusion Energy 2002, Proceedings of the 19th IAEA Conference*, Lyon, 2002 (IAEA, Vienna, EX/P1-13, 2003), Nucl. Fusion (submitted).